D. ELECTRONIC STRUCTURES OF REDUCED AND SUPERREDUCED Ir_2(1,8-diisocyanomenthane)$_4^{n+}$ COMPLEXES

Reprinted with permission from Záliš, S; Hunter, B. M.; Gray, H. B.; Vlček Jr, A. Electronic Structures of Reduced and Superreduced Ir_2(1,8-diisocyanomenthane)$_4^{n+}$ Complexes. *Inorganic Chemistry*, **2017**, *56*, 2874. DOI: 10.1021/acs.inorgchem.6b03001.

D.1. Abstract

Molecular and electronic structures of Ir_2(1,8-diisocyanomenthane)$_4^{n+}$ (Ir(dimen)$^{n+}$) complexes have been investigated by DFT for n = 2, 1, 0 (abbreviated **2+**, **1+**, **0**). Calculations reproduced the experimental structure of **2+**, ν(C≡N) IR, and visible absorption spectra of all three oxidation states, as well as the EPR spectrum of **1+**. We have shown that the two reduction steps correspond to successive filling of the Ir–Ir pσ orbital. Complexes **2+** and **1+** have very similar structures with **1+** having a shorter Ir–Ir distance. The unpaired electron density in **1+** is delocalized along the Ir–Ir axis and over N atoms of the eight C≡N– ligands. The second reduction step **1+** → **0** changes the Ir(CN–)$_4$ coordination geometry at each Ir site from approximately planar to seesaw whereby one –N≡C–Ir–C≡N– moiety is linear and the other bent at the Ir (137°) as well as N (146°) atoms. Although complex **0** is another example of a rare $(p\sigma)^2$ dimetallic species (after $[Pt_2(\mu\text{-}P_2O_5(BF_2)_2)_4]^{6-}$, *J. Am. Chem. Soc.* **2016**, *138*, 5699), the redistribution of lower-lying occupied molecular orbitals increases electron density predominantly at the bent C≡N– ligands whose N atoms are predicted to be nucleophilic reaction centers.

D.2. Introduction

Although the electronic excited states of binuclear complexes of d^8 metals (Pt^{II}, Ir^{I}, Rh^{I}) are versatile redox agents,[1,2,3,4,5,6,7,8,9,10] d^8-d^8 electrochemistry has not been studied in depth.[3,11,12,13,14,15,16,17,18,19,20] Investigating electrochemical reduction of d^8-d^8 complexes is challenging, owing to negative reduction potentials and slow heterogeneous electron transfer, as well as complications attributable to product reactivity. Indeed, reversible electrochemical reductions along with characterization of products have only been reported for $[Ir_2(1,8\text{-diisocyanomenthane})_4]^{2+}$ ($Ir(dimen)^{2+}$, abbreviated **2**+)[12] and $[Pt_2(P_2O_5(BF_2)_2)_4]^{4-}$ ($Pt(pop\text{-}BF_2)^{4-}$).[11] Notably, the $Ir(dimen)^{2+}$ complex was found to catalyze electrochemical reduction of CO_2.[13]

Both complexes are reduced in two chemically reversible 1-electron steps: **2**+ at -1.36 and -1.54 V vs. Ag/AgCl (ca. -1.75, -1.93 V vs. Fc^+/Fc);[12,13] $Pt(pop\text{-}BF_2)^{4-}$ at -1.68 and -2.46 V (vs. Fc^+/Fc).[11] For both complexes, the first reduction is chemically reversible, whereas the second one is quasireversible. A combined spectroelectrochemical (UV-vis absorption, EPR) and DFT-computational study of the $Pt(pop\text{-}BF_2)^{n-}$ redox series (n = 4, 5, 6) revealed that the two reduction processes correspond to successive filling of a Pt-Pt bonding pσ orbital (the LUMO of the parent complex).[11] Therefore, the Pt-Pt bonding strengthens upon the first and, even more, the second reduction. The superreduced complex is a very rare $6p^2$ σ-bonded binuclear complex; formally it is a dimer of Pt^{I} ($5d^86p^1$) rather than ($5d^9$).[11] While the calculations revealed small angular distortions around the metal atoms, the two Pt centers were found to be essentially equivalent with respective natural charges differing by only 0.035 e^-.[11]

By analogy, similar localization accompanying reduction processes could be expected for the $Ir(dimen)^{n+}$ redox series (n = 2, 1, 0). Indeed, the EPR spectrum of $Ir(dimen)^+$ (**1**+) and its IR spectrum in the range of C≡N– stretching vibrations, ν(C≡N), point to a $(p\sigma)^1$ configuration with an axial spin density distribution and an increased Ir→C≡N– π back donation, the latter manifested by a 66 cm^{-1} downshift of the ν(C≡N) IR band, from 2156

cm^{-1} in **2+** to 2090 cm^{-1} in **1+**.[12] The second reduction, however, was accompanied by a large (~189 cm^{-1}) splitting of the ν(C≡N) band into two new features (2058 and 1869 cm^{-1}).[12] Such behavior signals a loss of symmetry and formation of two distinct sets of isocyanide groups in the superreduced complex $Ir(dimen)^0$ (**0**). It was interpreted[12] as indicating asymmetry between the two metal centers; and **0** was formulated as a d^8-d^{10} ($Ir^{I}\cdots Ir^{-I}$) mixed-valence complex with approximately square planar and tetrahedral coordination geometries around Ir^{I} and Ir^{-I} centers, respectively.[12] The experimentally demonstrated asymmetry and the mixed-valence formulation of **0** are in stark contrast with the nearly symmetrical $(p\sigma)^2$ bond established[11] for $Pt(pop\text{-}BF_2)^{6-}$, thereby challenging our understanding of the electronic structures of superreduced d^8-d^8 complexes. We have therefore addressed the problem of bonding and electron localization in the $Ir(dimen)^{n+}$ redox series by DFT calculations.

D.3. Computational details

Electronic structures of $Ir(dimen)^n$ (n = 0, 1 and 2) in various oxidation states were calculated by DFT using the Gaussian 09 (G09) program package. The open shell system **1+** was calculated by the UKS approach. Geometry optimization was followed by vibrational analysis in order to characterize stationary states. Calculations performed without any symmetry constraints provided real energy minima for all investigated isomers and oxidation states. The short/twisted **2+** isomer was also optimized within the D_2 symmetry and the results were used to characterize the approximate symmetries of ν(C≡N) modes. DFT calculations employed the Perdew, Burke, Ernzerhof (PBE0) hybrid functional,[21,22] with the D3 version of Grimme's dispersion correction added.[23] (The choice of the PBE0 functional was motivated by the good results it has provided for Pt d^8-d^8 dimers and other heavy-metal complexes.[11,24,25,26]) The MeCN solvent was described by the polarizable conductor model (PCM).[27] The following basis sets were used: for H double ζ 6-31g(d) basis set,[28] for C, N, and O atoms polarized triple ζ basis sets 6-311g(d)[29,30], and quasirelativistic effective core pseudopotentials and corresponding optimized set of basis functions for Ir.[31,32] Electronic transitions were calculated by time-dependent DFT (TDDFT). Mayer-Mulliken bond orders

were obtained by the NBO 6 program. Reported vibrational frequencies were scaled[33,34] by a factor of 0.956 that provided the best match with the experimental ν(CN) band of **2**+. the same scaling factor was used for all there oxidation states.

D.4. Results

Isomerism

Two kinds of isomerism should be considered when dealing with Ir(dimen)^n complexes: deformational and orientational. Deformational isomerism arises from two possible combinations of Ir-Ir bond-lengths and ligand conformations, giving rise to long/eclipsed and short/twisted configurations[35,36,37] (Figure D.1) with distinctly different visible absorption spectra.[36,37] As both isomers are present in solution at room temperature,[36,37] they must be considered separately. Calculations were therefore performed on both deformational isomers in MeCN (modeled as a dielectric continuum). Gibbs free energies of the two **2**+ isomers were comparable (in MeCN, 298 K), with the long/eclipsed one more stable by 0.105 eV. However, its zero-point corrected electronic energy was calculated to be 0.029 eV higher than that of the short/twisted isomer, indicating stabilization of the short/twisted form with decreasing temperature, in agreement with experiment[36] ($\Delta H^o_{long\text{-}short}$ = +0.035 eV).

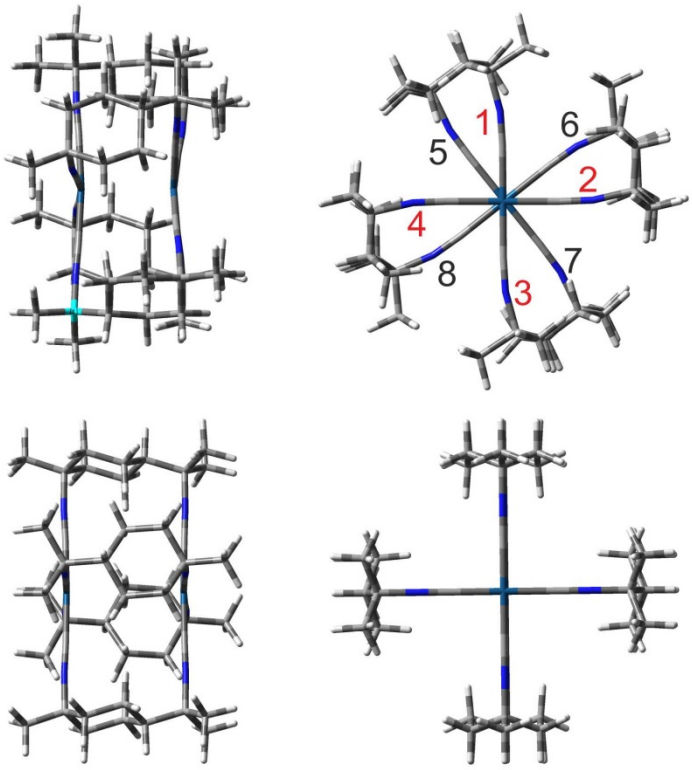

Figure D.1. DFT-optimized solution structures of short/twisted (top) and long/eclipsed (bottom) deformational isomers of the *trans*-2:2 orientational isomer of Ir(dimen)$^{2+}$ (further abbreviated **2**+). Left: side views; right: front views along the Ir-Ir (*z*) axis. The CN groups labeled 1,2,3,4 (red) are in the front, the 5,6,7,8 (black) ones are in the back.

Structure optimization of the short/twisted **2**+ isomer required the dispersion correction GD3,[38] otherwise the calculation did not converge. Hence, the GD3 correction was used throughout this work. A good match between calculated (Table D-1) and experimental[39] (3.60 and 4.3 Å, in MeCN solution) Ir–Ir distances was obtained for the two **2**+ deformational isomers. (Only the structure of the long/eclipsed isomer was successfully optimized without dispersion but the calculated bond length of 4.78 Å grossly overestimated the Ir–Ir distance. This result further underlines the importance of including dispersion in calculations of isocyanide d^8-d^8 complexes.[10,40])

Since the dimen ligand is asymmetric, the individual bridging ligands can adopt different "head-to-tail" relative orientations: 4:0 (all aligned), 3:1, *cis*-2:2, and *trans*-2:2. The respective DFT-calculated free energies of **2**+ orientational isomers (relative to the most stable isomer, MeCN, 293 K) are 0.077, 0.011, 0.003, and 0.0 eV for the long/eclipsed deformational isomer and 0.005, 0.0, 0.049, and 0.032 eV for the short/twisted isomer. The actual solution composition is not known and may vary with synthetic conditions. Crystal structures[35] show disordered dimen orientations, which correspond to mixtures of orientational isomers. Below, we present computational results for the *trans*-2:2 isomer obtained without any symmetry constraints. Calculations on other orientational isomers yielded very similar electronic structures, UV-vis and IR spectra.

Molecular structures

Both **2**+ isomers have typical d^8-d^8 structures, as there are two parallel, almost planar IrC_4 moieties (Figure D.1, Table D-1). The long/eclipsed and short/twisted isomers differ in the Ir–Ir distance and the twist angle between the two planes, calculated as 4.319 Å/0° and 3.244 Å/38.4°, respectively. The Ir-Ir distances match well the corresponding experimental values of 4.3 and 3.60 Å determined[39] in MeCN solution by X-ray scattering. The calculated twist angle is about twice as large as in the crystal structures,[35] indicating constraints imposed in the solid state. The deviation of IrC_4 units from planarity was calculated to be slightly larger in the long/eclipsed isomer (2.6-3.4°), which is different for the two *trans* pairs of dimen ligands (Table 1). The Ir–C≡N– units are essentially linear around the carbon atom but slightly bent at nitrogen atoms (more in the short/twisted isomer due to higher ligand strain).

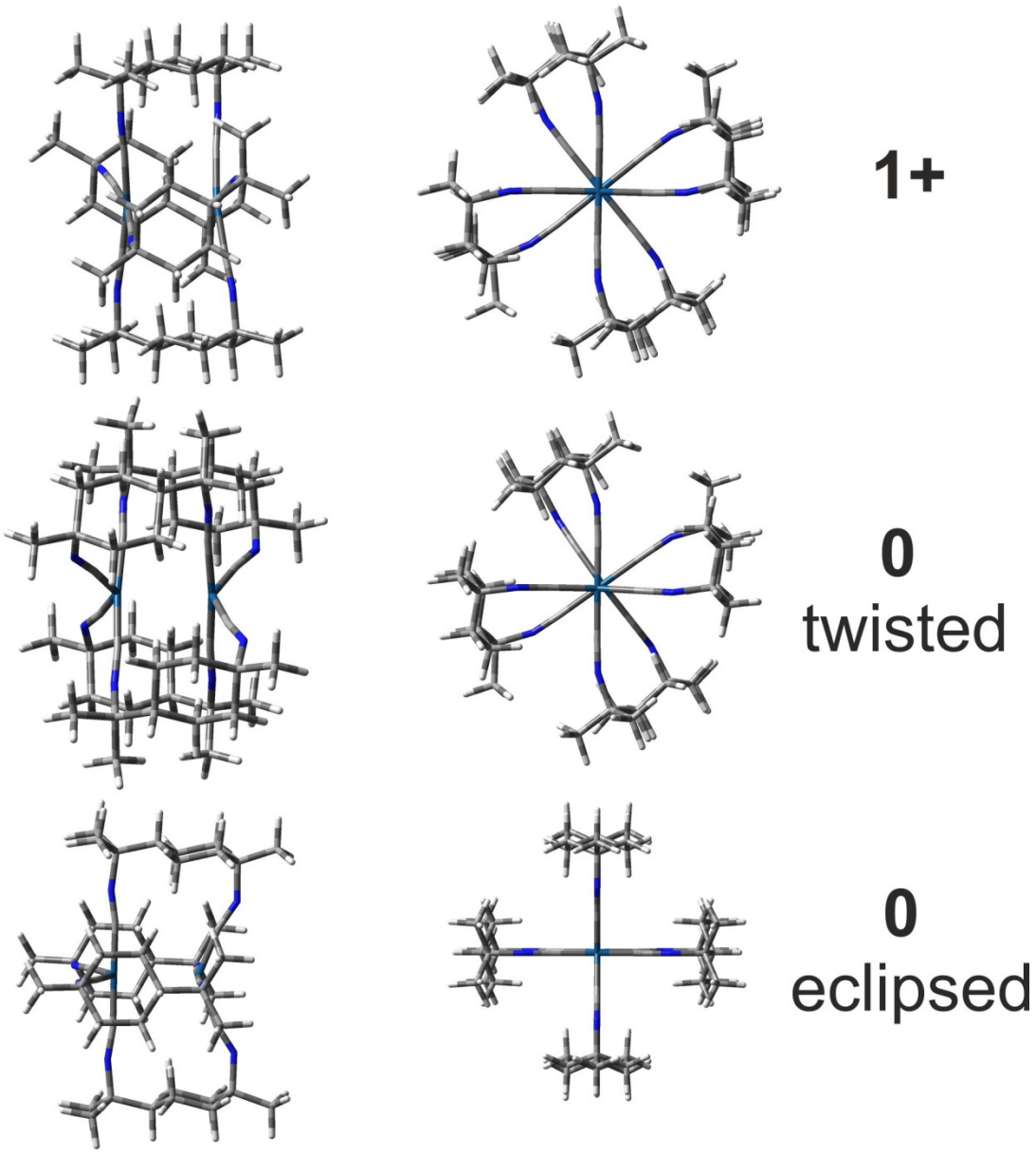

Figure D.2. Optimized molecular structures of $Ir(dimen)^{+}$ (top, further abbreviated **1**+) and the two deformational isomers of $Ir(dimen)^{0}$ (middle and bottom, further abbreviated **0**). Left: side views; right: front views along the Ir-Ir (*z*) axis.

Only a single stable structure (Figure D.2) was found for **1**+, whether or not optimization started from the short/twisted or long/eclipsed **2**+ structure. The first reduction triggers only small structural changes, especially when compared to the short/twisted isomer

of the parent. The IrC_4 units of **1+** remain nearly planar and parallel, although the deviation from planarity increases slightly to 3.7-5.1° (Table 1). The Ir–Ir distance shortens by 0.16 and 1.23 Å relative to the short/twisted and long/eclipsed **2+** isomers. The twist angle stays nearly the same. All the C≡N bonds lengthen and Ir–C bonds shorten by ca. 0.01 Å upon the first reduction.

The second reduction is accompanied by profound structural changes (Figure D.2, Table D-1). The IrC_4 geometry changes at each center from approximately square planar to seesaw. Two sets of $Ir(C{\equiv}N{-})_2$ units with different C-Ir-C angles as well as Ir–C and C≡N bond lengths occur in the **0** structure: axial, which are nearly linear and comparable to those in **1+**; and equatorial with a 137° angle between the Ir–C bonds. Equatorial Ir–C and C≡N bonds are ~0.03 Å shorter and longer, respectively, than in the axial unit. Moreover, equatorial isocyanide ligands are bent at the N atoms, with C≡N– angles ~20° smaller than in the axial ligands. DFT optimization yielded two stable isomeric structures of **0** that differ in the relative orientation of axial and equatorial positions at the two Ir centers (Figure B.2). In the twisted isomer, the IrC_4 units are twisted by 37.3°. The eclipsed isomer has the two seesaw sites perpendicular to each other, which leads to aligned –N≡C–Ir–C≡N– bonds when viewed along the Ir–Ir axis (Figure D.2). (In particular, the axial –N≡C–Ir–C≡N– moiety at one Ir is aligned with the equatorial unit at the other.) The calculated Ir–Ir bond length is similar in eclipsed (3.088 Å) and twisted (2.988 Å) isomers. In both cases, one C≡N– group of each dimen ligand is bound equatorially to one Ir atom while the other is bound axially to the second Ir. The twisted isomer was calculated to be more stable by 0.029 eV in MeCN at 298 K.

Table D-1: DFT-calculated Ir(dimen)$^{n+}$ structural parameters. Bond lengths in Å. Atom numbering is shown in Figure B.1.

Bond / n	**2+$_{long/ecl}$**	**2+$_{short/tw}$**	**1+**	**0$_{eclipsed}$**	**0$_{twisted}$**
Ir1-Ir2	4.319	3.251	3.087	3.088	2.988
Ir-C1	1.959	1.959	1.949	1.945 [ax]	1.943 [ax]
Ir-C2	1.959	1.959	1.949	1.917 [eq]	1.923 [eq]
Ir-C3	1.959	1.959	1.949	1.945 [ax]	1.943 [ax]
Ir-C4	1.959	1.959	1.949	1.917 [eq]	1.923 [eq]
Ir-C5	1.959	1.959	1.949	1.945 [ax]	1.943 [ax]
Ir-C6	1.959	1.959	1.949	1.917 [eq]	1.923 [eq]
Ir-C7	1.959	1.959	1.949	1.945 [ax]	1.943 [ax]
Ir-C8	1.959	1.959	1.949	1.917 [eq]	1.923 [eq]
C_a-N_a	1.161 [a]	1.163 [a]	1.171 [a]	1.197 [ax]	1.196 [ax]
C_b-N_b	1.161 [b]	1.163 [b]	1.170 [b]	1.174 [eq]	1.175 [eq]
angle					
Ir2-Ir1-C1	90.8	92.6	93.8	89.7 [ax]	87.2 [ax]
Ir2-Ir1-C2	90.8	93.4	94.5	111.5 [eq]	109.2 [eq]
Ir2-Ir1-C3	90.8	92.6	93.7	89.7 [ax]	87.2 [ax]
Ir2-Ir1-C4	90.8	93.4	94.6	111.5 [eq]	109.2 [eq]
Ir2-Ir1-C5	90.8	92.6	95.1	111.5 [eq]	109.2 [eq]
Ir2-Ir1-C6	90.8	93.4	94.0	89.7 [ax]	87.2 [ax]

Ir2-Ir1-C7	90.8	92.6	95.2	111.5 [eq]	109.2 [eq]
Ir2-Ir1-C8	90.8	93.4	94.0	89.7 [ax]	87.2 [ax]
C_a-N_a-C	176.9 [a]	168.2 [a]	165.2 [a]	165.2 [ax]	161.5 [ax]
C_b-N_b-C	177.4 [b]	168.8 [b]	166.0 [b]	145.2 [eq]	146.2 [eq]
C_a-Ir1-Ir2-$C_{a'}$ [c]	0.0	38.4	40.4	0.0	37.3
C_b-Ir1-Ir2-$C_{b'}$ [d]	0.0	38.4	39.9	0.0	37.3

[a] Average of C1N1, C3N3, C5N5, and C7N7 distances or corresponding C-N-C angles. [b] Average of C2N2, C4N4, C6N6, and C8N8 distances or corresponding C-N-C angles. [c] Average of C1Ir1Ir2C5 and C3Ir1Ir2C7 angles. [d] Average of C2Ir1Ir2C6 and C4Ir1Ir2C8 angles. Superscript ax refers to the axial –N≡C–Ir–C≡N– linkage of the seesaw structure (Figure D.2); eq refers to the equatorial (bent, 137°) Ir(C≡N–)$_2$ moiety of the seesaw structure (Figure D.2).

Infrared spectra: ν(C≡N) vibrations

DFT-calculations closely reproduced experimental IR spectra in the ν(C≡N) region of all three redox states of Ir(dimen)$^{n+}$, in terms of peak wavenumbers as well as relative intensities and, hence, also the isosbestic points (Figure D.3 and Table D-2). Corresponding vibrational motions are depicted in Figure D.4. Experimental IR bands are broader and show several weak shoulders, usually on their low-energy sides (Figure D.3-left). These features are attributable to the presence of several nearly degenerate modes, the two deformational isomers, as well as to contributions from various orientational isomers whose IR spectra were calculated to be very similar.

The single ν(C≡N) band displayed by **2**+ arises from almost degenerate B_3 and B_2 vibrations in the approximate D_2 symmetry (originating from an E_u mode in D_{4h}). These

vibrations correspond to antisymmetric combinations of C≡N stretchings (Figure D.4). The first reduction shifts[12] this band by -66 cm^{-1}, which is matched by the calculated shift of -59 cm^{-1} relative to the short/twisted isomer (-74 cm^{-1} with respect to the long/eclipsed isomer). The calculated **1**+ spectrum shows a peak at 2094 cm^{-1} and a shoulder at 2122 cm^{-1} that also is apparent on the high-energy side of the experimental band (Figure D.3). The main peak results from downshifted B_3 and B_2 ν(C≡N) vibrations, while the shoulder is due to a mode calculated for **2**+ at 2212 cm^{-1} that gains IR intensity owing to a small distortion upon reduction.

As in the spectroelectrochemical experiment,[12] the DFT-simulated IR spectral pattern changes upon reduction to **0**. Two ν(C≡N) bands emerge at ca. 2068 and 1897 cm^{-1} with a distinct shoulder at ~1920 cm^{-1} that match experimental features at 2058 and 1867-1883 cm^{-1}, together with a ~1915 cm^{-1} shoulder (Figure D.3). The higher band is due to closely spaced C≡N stretching vibrations of axial (linear) –N≡C–Ir–C≡N– moieties at both Ir centers, whereas the lower band corresponds to similar vibrations of equatorial (bent) $Ir(C{\equiv}N{-})_2$ units. The calculations indicated only very little mixing between stretching motions of the two kinds of C≡N– ligands. The most IR-active vibrations of both deformational isomers are shown in Figure B.4. The calculated splitting of the two main ν(C≡N) IR features (172 cm^{-1}, on the average) is very near the experimental value of 189 cm^{-1}.[12]

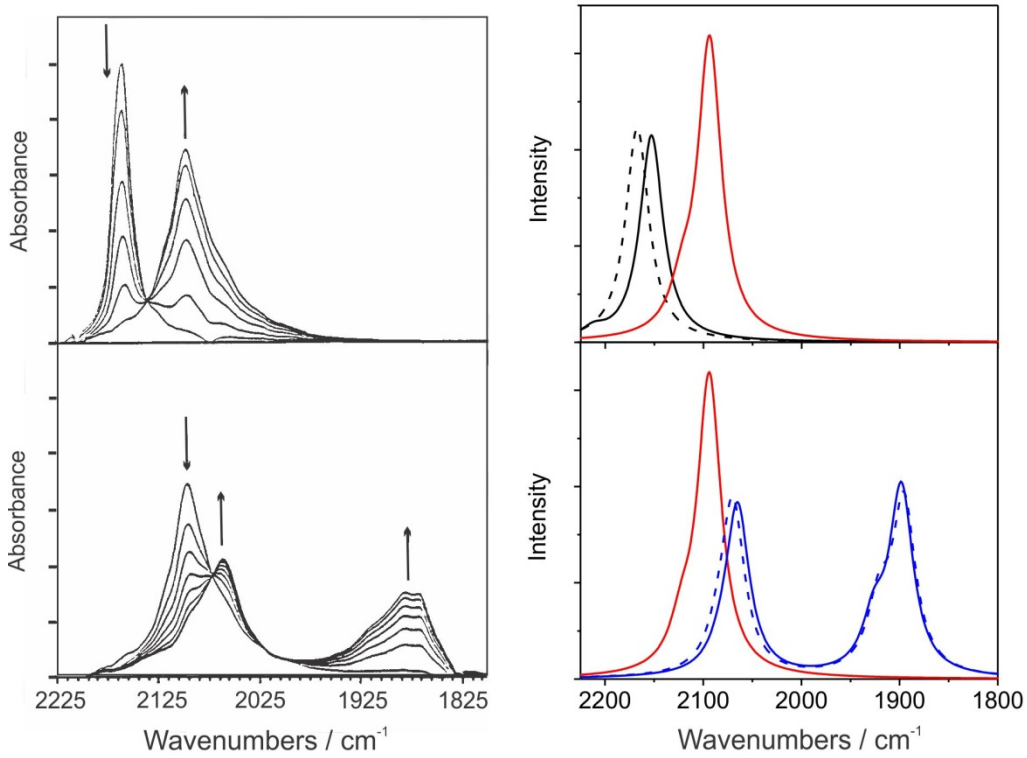

Figure D.3 Left: Experimental spectra recorded in MeCN during **2**+ → **1**+ (top) and **1**+ → **0** (bottom) electrochemical reductions. (Adapted with permission from ref.[12] Copyright (1993) American Chemical Society.) Right: calculated ν(C≡N) IR spectra of **2**+ (black), **1**+ (red), and **0** (blue) in MeCN. Full lines: short/twisted isomers, dashed lines: long/eclipsed isomers. Simulated spectra assumed fwhm of 30 cm^{-1}.

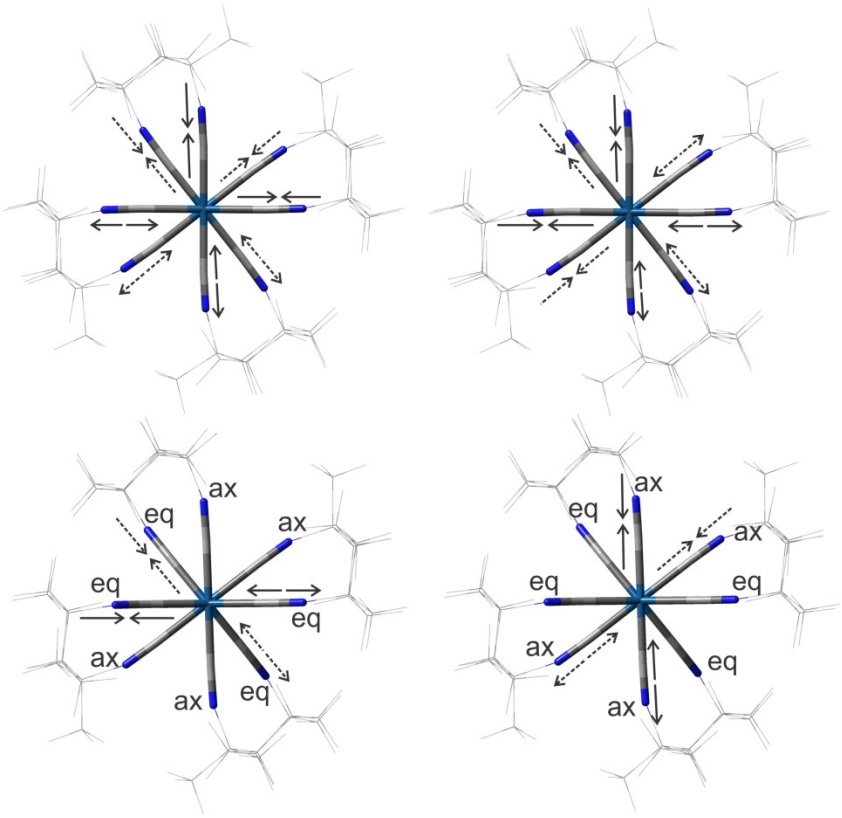

Figure D.4. Top: Schematic representation of DFT-calculated B_3 and B_2 ν(C≡N) vibrations of short/twisted **2**+, both calculated at 2168 cm^{-1}. Bottom: most intense ν(C≡N) vibrations of twisted **0** calculated at 1897 cm^{-1} (left) and 2066 cm^{-1} (right). Views of the structures are in the direction of the Ir–Ir bond. Labels ax, eq denote the axial (linear) and equatorial (bent) ligands, respectively. Full and dashed arrows indicate vibrational motions of the front and back parts of the molecule, respectively.

Table D-2: DFT calculated ν(C≡N) wavenumbers (cm^{-1}) and intensities (in parenthesis, 10^3 km/mol) of **2**+, **1**+, and **0**. Wavenumbers are scaled by 0.956. Experimental data from ref.[12]

2+			**1**+		**0**		
long/ecl	short/tw	Exp.	Calc.	Exp.	eclipsed	twisted	Exp.
2164 (0.2)	2147 (0.0)		2088		1896 (4.8)	1897 (8.4)	1867-1883[a]
2164 (0.0)	2147 (0.0)		2088 (0.7)		1896 (4.8)	1902 (2.2)	
2168 (6.0)	2153 (5.7)	2156	2092 (0.0)		1921 (3.6)	1926 (2.8)	1915 sh
2168 (5.9)	2153 (5.9)		2094 (8.3)	2090	1938 (0.0)	1944 (0.0)	
2188 (0.0)	2170 (0.0)		2095 (7.9)		2070 (4.8)	2063 (2.8)	2058
2190 (0.0)	2172 (0.0)		2096 (0.0)		2070 (4.8)	2066 (6.9)	
2240 (0.0	2212 (0.5)		2122 (2.1)	sh	2084 (1.2)	2082 (0.7)	sh
2243 (0.0)	2231 (0.0)		2187 (0.0)		1896 (0.0)	2132 (0.0)	

[a] Broad band with several apparent maxima, see Figure B.3-left. sh: shoulder apparent in the experimental spectrum.

Electronic structure: molecular orbitals and bonding

The MO diagram of **2**+ (Figure D.5) matches the qualitative bonding model proposed for d^8-d^8 complexes in 1975.[41] The $5d_z^2$ orbitals from each Ir atom combine in bonding and antibonding fashion producing dσ and dσ* (HOMO) orbitals that are both occupied. A similar interaction between $6p_z$ orbitals leads to pσ (LUMO) and pσ* orbitals. The splitting between σ bonding and antibonding orbitals is very small in the long/eclipsed isomer but increases on going to the short/twisted isomer, as the Ir–Ir distance shortens. A manifold of occupied 5dπ/π(CN) orbitals is at lower energies (Figure D.5). Although Ir–Ir σ bonding and

antibonding pairs of orbitals are either occupied or empty and no net bonding is expected, the Mayer-Mulliken bond orders indicate a weak bonding interaction: 0.072 (long/eclipsed) and 0.156 (short/twisted). Dispersion forces between the two parallel $Ir(C{\equiv}N{-})_4$ planes further stabilize the dimeric structure,[10,40] as discussed above.

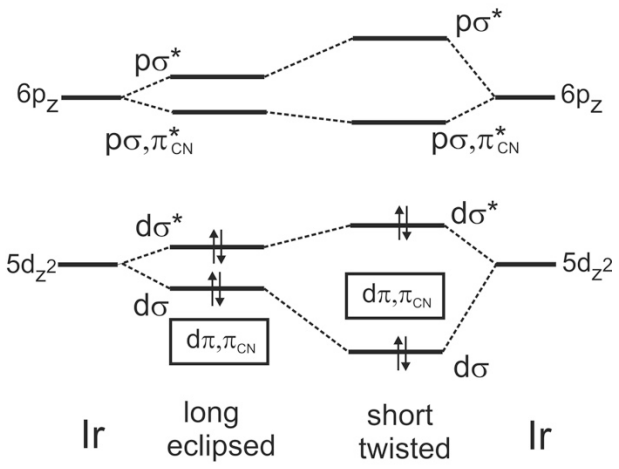

Figure D.5. Qualitative MO scheme of **2+**. dπ orbitals are π bonding or antibonding with respect to the Ir–Ir bond.

The MOs relevant to Ir–Ir bonding are shown in Figure D.6. Importantly, the **2**+ pσ LUMO is delocalized over the C≡N– groups whose π* orbitals contribute ca. 60 % while the $6p_z$ contribution was calculated to be ca. 35%. (A calculation with forced molecular symmetries indicated even larger delocalization with ~20% $6p_z$ participation.[36]) DFT calculations of the reduced and superreduced forms show that both reduction steps involve successive filling of the pσ LUMO orbital, with only minor changes in its composition.

For **1**+, the pσ-localization of the extra electron is supported by the calculated spin density distribution that approximately coincides with the pσ SOMO shape and produces EPR parameters (g_1 = 2.047, g_2 = 2.043, g_3 = 1.991) close to the experimental values[12] (g_1 = 2.064, g_2 = 2.060, g_3 = 2.01), maintaining the relation $g_1 \approx g_2 > g_3$ that reflects axial symmetry.

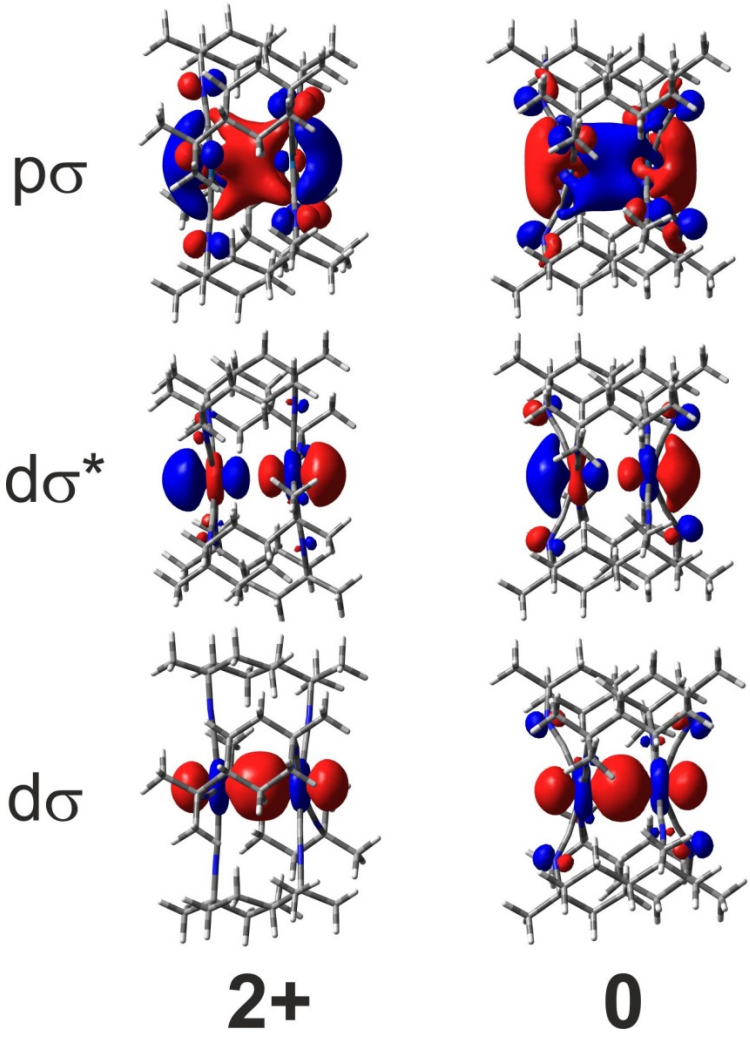

Figure D.6. Shapes of dσ, dσ*, and pσ orbitals of short/twisted isomers of **2**+ and **0**.

Lower-lying occupied orbitals of **2**+ and **1**+ are predominantly Ir 5d in character, π or π* with respect to the Ir-Ir bond. They are partly delocalized over the ligands, much more on N than C atoms. Whereas the delocalization over the eight C≡N– groups is nearly even in **2**+ and **1**+, large differences between axial and equatorial C≡N– π orbitals were found for **0**, whereby C and N atoms of the equatorial C≡N– groups participate in HOMO-1,2,3 almost equally (~15%). The involvement of axial ligands is much smaller, and mostly through the N atoms, as in **2**+ and **1**+.

Further insight into bonding changes upon reduction is provided by Mayer-Mulliken bond orders (Table D-3). The Ir–Ir bond order slightly increases upon the first reduction: by 0.045 relative to short/twisted **2**+, whereas a larger change (0.129) was calculated with respect to the long/eclipsed isomer. Filling the pσ orbital in the course of the second reduction is accompanied by further Ir–Ir bond-order increase of ca. 0.1. All three redox states show an alternating pattern of Ir–C and C–N bond orders whereby the equatorial –N≡C–Ir–C≡N– moieties are characterized by higher Ir–C and lower C–N bond orders than the axial ones. While these differences are negligible in **2**+ and **1**+, they become pronounced in both superreduced isomers. Bond-order changes and corresponding axial/equatorial alternation thus indicate that the second reduction mainly affects equatorially-bound pairs of C≡N– groups at both Ir centers.

Table D-3: Mayer-Mulliken bond orders of Ir(dimen)$^{n+}$ (**2+**, **1+**, **0**) complexes. Labels ax, eq denote the axial (linear) and equatorial (bent) ligands, respectively.

bond \ n	**2+** long/eclipsed	**2+** short/twisted	**1+**	**0** twisted	**0** Eclipsed
Ir – Ir	0.072	0.156	0.201	0.286	0.311
Ir1 – C1	0.526	0.558	0.618	0.594 ^{ax}	0.622 ^{ax}
Ir1 – C2	0.523	0.568	0.635	0.940 ^{eq}	0.928 ^{eq}
Ir1 – C3	0.526	0.559	0.618	0.594 ^{ax}	0.622 ^{ax}
Ir1 – C4	0.523	0.568	0.635	0.940 ^{eq}	0.928 ^{eq}
C1 – N1	2.374	2.345	2.237	2.170 ^{ax}	2.193 ^{ax}
C2 – N2	2.375	2.345	2.236	2.035 ^{eq}	2.038 ^{eq}
C3 – N3	2.375	2.345	2.236	2.170 ^{ax}	2.193 ^{ax}
C4 – N4	2.374	2.345	2.450	2.035 ^{eq}	2.038 ^{eq}
Ir2 – C5	0.523	0.558	0.647	0.940 ^{eq}	0.928 ^{eq}
Ir2 – C6	0.526	0.568	0.621	0.594 ^{ax}	0.622 ^{ax}
Ir2 – C7	0.523	0.559	0.647	0.940 ^{eq}	0.928 ^{eq}
Ir2 – C8	0.524	0.568	0.622	0.594 ^{ax}	0.622 ^{ax}
C5 – N5	2.374	2.345	2.231	2.035 ^{eq}	2.038 ^{eq}
C6 – N6	2.375	2.345	2.237	2.170 ^{ax}	2.193 ^{ax}
C7 – N7	2.375	2.345	2.238	2.035 ^{eq}	2.038 ^{eq}
C8 – N8	2.374	2.345	2.436	2.170 ^{ax}	2.193 ^{ax}

Localization of the reduction steps can be examined by comparing changes of Mulliken charges upon the first and second reduction steps (Table D-4). The first reduction is delocalized over the Ir_2 unit (0.39 e^-, 0.2 e^- per Ir atom) and the eight C≡N– groups, where the electron density increases by 0.31 e^- (mainly at N, 0.23 e^-, 0.03 e^- per atom). There is virtually no difference between the two $Ir(C{\equiv}N{-})_4$ units and between axial and equatorial C≡N– groups. On the other hand, upon second reduction, the charge decreases by 0.15 e^- on both Ir atoms and by 0.48 e^- on all eight C≡N– units (twisted isomer), with a large difference between axial (-0.17 e^-) and equatorial (-0.31 e^-) ligands. This difference is even more pronounced in the eclipsed isomer: -0.08 vs. -0.37 e^-, respectively; and the charge on the two Ir atoms decreases by 0.19 e^-. The DFT-calculated charge changes also show that the electron density added in each reduction step is nearly equally distributed over the two $Ir(CN{-})_4$ units. In particular, the increases in electron density at Ir1 and Ir2 upon second reduction are virtually identical.

Table D-4: Changes of DFT-calculated Mulliken charges at individual atoms accompanying the two reduction steps of **2**+. The isomers are specified in parenthesis. Labels ax, eq denote the axial (linear) and equatorial (bent) ligands, respectively.

	2(sh/tw)→1	1→0(tw)	1→0(ecl)
Ir1	-0.194	-0.072	-0.092
C[a]	-0.011	-0.012 [ax]	-0.003 [ax]
N[a]	-0.029	-0.031 [ax]	-0.017 [ax]
C[b]	-0.009	-0.033 [eq]	-0.054 [eq]
N[b]	-0.030	-0.042 [eq]	-0.036 [eq]
Ir2	-0.193	-0.074	-0.093
C[c]	-0.005	-0.037 [eq]	-0.058 [eq]
N[c]	-0.030	-0.042 [eq]	-0.036 [eq]
C[d]	-0.011	-0.012 [ax]	-0.002 [ax]
N[d]	-0.028	-0.031 [ax]	-0.018 [ax]

[a] Average for C1 and C3, N1 and N3. [b] Average for C2 and C4, N2 and N4. [c] Average for C5 and C7, N5 and N7. [d] Average for C6 and C8, N6 and N8.

UV-vis absorption spectra

TDDFT-calculated electronic transitions for both **2**+ deformational isomers as well as for reduced and superreduced forms match the experimental spectra (Figure D.7 and Table D-5). The lowest absorption band of each **2**+ isomer originates from the HOMO→LUMO transition and, given the delocalized LUMO character, can be described as

$d\sigma^* \rightarrow p\sigma$/MMLCT (MMLCT = metal-metal to ligand charge transfer). The strong sharp bands in the UV region are $d\pi \rightarrow p\sigma$(LUMO), predominantly MMLCT. The position of the lower UV band (377-378 nm) matches the calculated triplet transitions at 367 and 384 nm while no spin-allowed transitions were calculated to fall in this region. We conclude that this band is attributable to a pair of close-lying spin-forbidden $^3d\pi \rightarrow p\sigma$ transitions, in accord with polarized absorption and MCD spectra of an analogous complex Ir_2(2,5-diisocyano-2,5-dimethylhexane)$_4^{2+}$.[42] As with $Pt(pop\text{-}BF_2)^{4-}$,[25] a full assignment of the Ir(dimen) UV spectrum will require calculation that includes spin-orbit coupling explicitly.

Electronic transitions of the open-shell complex **1**+ are described in terms of spin-orbitals. A weak low-energy band at 800 nm that appears upon the first reduction[12] is attributable to a βHOMO($d\sigma^*$)$\rightarrow\beta$LUMO($p\sigma$) transition (calculated at 713 nm). This feature is the counterpart of the $d\sigma^* \rightarrow p\sigma$ visible band of **2**+. A second, stronger band at 595 nm (calculated at 532 nm) is due to a αHOMO($p\sigma$)$\rightarrow\alpha$LUMO($p\sigma^*$/CN(π^*) transition of mixed MMLCT/intraligand character. In the UV region, **1**+ exhibits a band at 320 nm arising from two strongly mixed transitions. The experimental absorption spectrum of **0** exhibits[12] features at 432 nm (calculated at 411-425 nm) due to a HOMO($p\sigma$)$\rightarrow$LUMO($p\sigma^*$) transition and at 300 nm that include several transitions from HOMO($p\sigma$) and HOMO-1($d\sigma^*$) to LUMO and other high-lying orbitals (calculated at 306-328 nm).

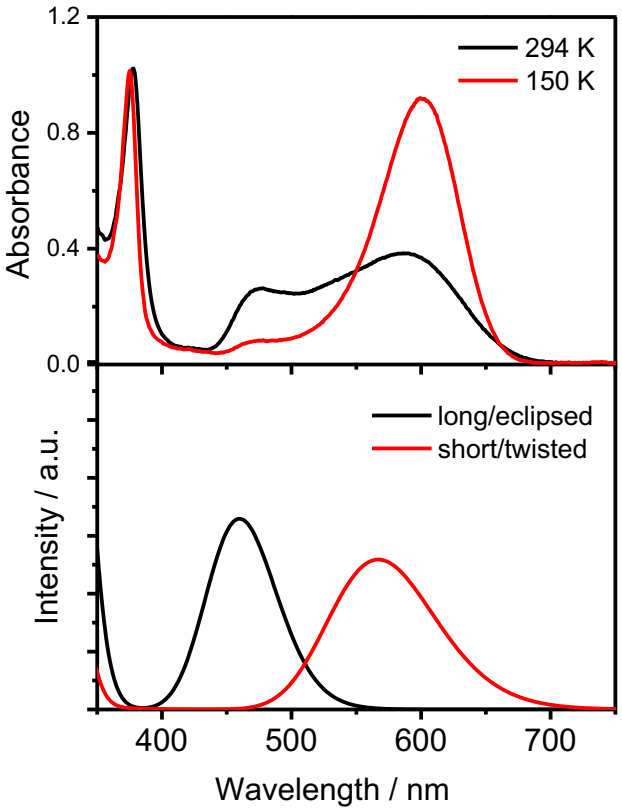

Figure D.7. Experimental UV-vis absorption spectra of **2**+ at 293.5 and 150 K (top) and simulated visible spectra of the long/eclipsed and short/twisted isomer (bottom). Simulated spectra assumed fwhm of 3000 cm^{-1}.

Table D-5: Calculated and experimental UV-vis spectra of $Ir(dimen)_4^n$ in MeCN. Transitions with oscillator strengths larger than 0.01 and spectroscopically relevant[42] triplet transitions (^3A) are listed.

Compound	Main contributing excitations (%)	Wavelength nm	Oscillator strength	Experiment λ, nm (ε, $M^{-1}cm^{-1}$)
2+ long/eclipsed	HOMO→LUMO (95)	460	0.227	475 [a]
	HOMO-4 →LUMO (95) ^3A	384	-	378 [a,d]
	HOMO-5 →LUMO (95) ^3A	384	-	
	HOMO-4 →LUMO (95)	326	0.376	327 [b] (36600)
	HOMO-5 →LUMO (95)	326	0.376	
2+ short/twisted	HOMO→LUMO (99)	567	0.178	598 [c] (7300 [b])
	HOMO-3 →LUMO (99) ^3A	367	-	377 [c,d] (18000 [b])
	HOMO-4 →LUMO (99) ^3A	366	-	
	HOMO-3 →LUMO (99)	321	0.177	327 [b] (36600)
	HOMO-4 →LUMO (99)	320	0.201	
1+	βHOMO→βLUMO (86)	713	0.019	800 [b] (3700)
	αHOMO→αLUMO (81)	534	0.211	595 [b] (12300)
	αHOMO→αLUMO+8 (60)	350	0.019	
	mixed	320	0.204	320 [b] (20900)
	mixed	320	0.246	
0 twisted	HOMO→LUMO+2 (96)	443	0.014	432 [b] (14400)
	HOMO→LUMO (98)	425	0.305	
	HOMO→LUMO+5 (94)	384	0.019	
	HOMO→LUMO+4 (97)	383	0.013	

	HOMO→LUMO+7 (89)	334	0.021	
	HOMO→LUMO+8 (89)	328	0.138	300 [b] (25100)
	HOMO→LUMO+10 (95)	317	0.037	
	HOMO-1→LUMO (90)	306	0.093	
0 eclipsed	HOMO→LUMO (99)	441	0.347	432 [b] (14400)
	HOMO→LUMO+2 (96)	411	0.011	
	HOMO→LUMO+5 (94)	368	0.008	
	HOMO→LUMO+4 (97)	368	0.009	
	HOMO→LUMO+8 (89)	322	0.113	300 [b] (25100)
	HOMO-1→LUMO (90)	322	0.113	
	HOMO→LUMO+10 (95)	317	0.037	

[a] 293.5 K; from ref.[39], [b] room temperature; from ref.[12], [c] 150 K; from ref.[39], [d] Assigned as $d_{xz,yz} \rightarrow p\sigma\ ^3E_u$ transition.[42]

D.5. Discussion

Our DFT calculations account for spectral changes in the **2+**, **1+**, **0** redox series; they also reveal changes of the molecular and electronic structures accompanying the two reduction steps. The reduction process can be interpreted as a sequential filling of the **2+** pσ LUMO. It is accompanied by large molecular and electronic relaxation upon addition of the second electron in the **1+** → **0** step.

The first reduction **2+** → **1+** amounts to simple electron addition to the pσ orbital in accord with the axial EPR spectrum of **1+**. The extra electron (spin) density is localized along the Ir-Ir linkage (Figure S2) and the eight N atoms. The UV-vis spectrum retains the dσ*→pσ band accompanied by a new feature at higher energy due to excitation of the pσ

electron to the pσ* orbital. The ν(C≡N) IR spectral pattern of **2**+ (single band) is preserved in **1**+, in agreement with the calculated **1**+ structure (Table D-1). The 66 cm^{-1} downshift of the ν(C≡N) band is attributable to electron delocalization over the isocyanide ligands that arises from overlap of the Ir $6p_z$ with π*(C≡N–) orbitals. It also accords with the ~0.01 Å lengthening of C≡N bonds. Bond orders (Table D-3) indicate that the eight Ir–C≡N– units are very similar.

Addition of the second electron to the pσ orbital causes a major change in both molecular and electronic structures although the character of the pσ orbital changes very little on going to **0** and its double occupancy amounts to formation of a $(p\sigma)^2$ bond as in $[Pt(pop\text{-}BF_2)]^{6-}$.[11] Accordingly, the Ir-Ir distance in **0** is shorter and the bond order is larger than in **1**+. Of importance is that the planar $Ir(C{\equiv}N{-})_4$ arrangement is unstable upon the second reduction; and a seesaw geometry is adopted at both Ir centers. (Alternatively, each Ir site can be viewed as trigonal bipyramidal, whereby the two axial and two of the equatorial positions are occupied by C≡N– groups and the other Ir atom occupies the third equatorial site.) Two nonequivalent –N≡C–Ir–C≡N– groups are at each Ir center: axial (linear), and equatorial that are bent at both Ir and N atoms and characterized by relatively large Ir–C and low C≡N bond orders (Table D-3). Axial bonds essentially retain their Ir–C≡N– character, only slightly modified by increased π back donation due to full pσ occupation. The nonequivalence of the two kinds of C≡N– groups in **0** accounts for the most striking spectroelectrochemical feature in the $Ir(dimen)^{n+}$ series: the large splitting of the ν(C≡N) IR band upon second reduction. The two IR bands of **0** correspond to antisymmetric stretching vibrations of axial and equatorial –N≡C–Ir–C≡N– moieties. Relative to the single ν(C≡N) feature of **1**+, the axial and equatorial vibrations in **0** shift lower by 32 and ca. 215 cm^{-1}, respectively, reflecting larger electron density localization at equatorial C≡N– groups.

Despite the pσ localization of the extra electron in **0**, the electron density increase relative to **1**+ is much larger on the equatorial than on the axial CN– groups and the Ir atoms (Table D-4). This is because the **1**+ → **0** reduction is accompanied by enhanced

delocalization of some of the lower-lying occupied MOs over the equatorial CN– groups. In consequence, the overall electron density increase on the four equatorial CN– ligands is more than two times larger than on both Ir atoms. It is worth noting that both reduction steps are accompanied by large electron density increases at the N atoms, especially on the bent equatorial ligands (0.07 e^- at each N_{eq}, relative to **2**+). The superreduced complex **0** thus possesses two kinds of nucleophilic centers (Ir and N_{eq}) that could play roles in substrate activation. Indeed, electrochemical CO_2 and H_2O reduction catalyzed by **2**+ has been reported.[13]

Relaxation of molecular and electronic structures upon the second reduction stabilizes the superreduced species **0** by delocalizing electron density over the whole molecule. The structural flexibility of the dimen ligand and the π-accepting ability of isocyanide groups are key factors in allowing this stabilization. In the case of isoelectronic $Pt(pop\text{-}BF_2)^{6-}$, such relaxation is limited by the rigidity of the pop-BF_2 ligand cage.[11] The lack of stabilizing reorganization of the superreduced Pt complex leads to a larger difference between the first and second reduction potentials (ΔE = -0.78 V) as well as the much more negative second reduction potential (E_2 = -2.46 V) than in the case of the Ir complex (ΔE = -0.18, E_2 = -1.93 V, respectively, even though the first reduction potentials are similar: -1.68 V (Pt), -1.75 V (Ir)).

D.6. Conclusions

Our DFT calculations accord with the experimental structure of **2**+, as well as the EPR spectrum of **1**+ and the ν(C≡N) IR and visible absorption spectra of all three $Ir(dimen)^{n+}$ complexes (**2**+, **1**+, **0**). We have found that dispersion forces between the $Ir(CN–)_4$ planes contribute to the stability of the dimeric structure. The two reduction steps correspond to successive filling of a pσ orbital that is delocalized over the C≡N– ligands. **0** is another example of a $(p\sigma)^2$-bonded dimer, after $Pt(pop\text{-}BF_2)^{6-}$.[11]

Structural changes accompanying **2**+ to **1**+ reduction are very small. The extra electron density (spin density) is delocalized in the direction of the molecular axis between the two Ir

atoms, at the outer sides of the IrC_4 planes, and over the N atoms of the eight C≡N– groups. The second reduction (**1+** to **0**) triggers a profound structural change that produces two non-equivalent sets of C≡N– ligands, axial and equatorial, but maintains the near-equivalence of the two Ir centers. The extra electron density is delocalized mainly over the four equatorial C≡N– groups that are bent at the N atoms. The prediction that equatorial N atoms could act together with Ir atoms as nucleophilic centers provides motivation for our forthcoming electrocatalytic studies employing $Ir(dimen)^{n+}$ complexes.

D.7. References and Notes

1. Yam, V. W.-W.; Au, V. K.-M.; Leung, S. Y.-L., Light-Emitting Self-Assembled Materials Based on d^8 and d^{10} Transition Metal Complexes. *Chem. Rev.* **2015** *115*, 7589−7728.

2. Roundhill, D. M.; Gray, H. B.; Che, C.-M., Pyrophosphito-Bridged Diplatinum Chemistry. *Acc. Chem. Res.* **1989,** *22*, 55-61.

3. Harvey, P. D., Chemistry, properties and applications of the assembling 1,8-diisocyano-p-menthane, 2,5-dimethyl-2,5-diisocyanohexane and 1,3-diisocyanopropane ligands and their coordination polynuclear complexes. *Coord. Chem. Rev.* **2001,** *219–221*, 17–52.

4. Sweeney, R. J.; Harvey, E. L.; Gray, H. B., Photoreactions of tetrakis(m-pyrophosphito)diplatinate(II) with alcohols and hydrocarbons. *Coord. Chem. Rev.* **1990,** *105*, 23-34.

5. Smith, D. C.; Gray, H. B., Photochemistry of Binuclear d^8 Complexes. *Coord. Chem. Rev.* **1990,** *100*, 169-181.

6. Marshall, J. L.; Stiegman, A. E.; Gray, H. B., Photochemistry of Dinuclear d^8-d^8 Iridium and Platinum Complexes. In *Excited States and Reactive Intermediates. ACS Symposium Series.*, Lever, A. B. P., Ed. American Chemical Society: Washington, DC, 1986; Vol. 307, pp 166-176.

7. Peterson, J. R.; Kalyanasundaram, K., Energy- and Electron-Transfer Processes of the Lowest Triplet Excited State of Tetrakis(diphosphito)diplatinate(II). *J. Phys. Chem.* **1985,** *89*, 2486-2492.

8. Heuer, W. B.; Totten, M. D.; Rodman, G. S.; Hebert, E. J.; Tracy, H. J.; Nagle, J. K., Electron-Transfer Reactions and Luminescent Quantum Yield of the Triplet Excited State of Tetrakis[m-diphosphito(2-)-*P*,*P*′]diplatinate(II). *J. Am. Chem. Soc.* **1984,** *106*, 1163-1164.

9. Milder, S. J.; Goldbeck, R. A.; Kliger, D. S.; Gray, H. B., Studies of Energy-Transfer and Electron-Transfer Processes Involving the $^3A_{2u}$ Excited States of Binuclear Rhodium Isocyanide Complexes. *J. Am. Chem. Soc.* **1980,** *102*, 6761-6764.

10. Gray, H. B.; Záliš, S.; Vlček, A., Electronic structures and photophysics of d^8-d^8 complexes *Coord. Chem. Rev.* **2017**, http://dx.doi.org/10.1016/j.ccr.2017.1001.1008.

11. Darnton, T. V.; Hunter, B. M.; Hill, M. G.; Záliš, S.; Vlček, A., Jr.; Gray, H. B., Reduced and Superreduced Diplatinum Complexes. *J. Am. Chem. Soc.* **2016,** *138*, 5699−5705.

12. Hill, M. G.; Sykes, A. G.; Mann, K. R., Spectroelectrochemical Characterization of $Ir_2(dimen)^{4+}$ and $Ir_2(dimen)_4^0$ (dimen = 1,8-Diisocyanomenthane). *Inorg. Chem.* **1993,** *32*, 783–784.

13. Cheng, S. C.; Blaine, C. A.; Hill, M. G.; Mann, K. R., Electrochemical and IR Spectroelectrochemical Studies of the Electrocatalytic Reduction of Carbon Dioxide by $[Ir_2(dimen)_4]^{2+}$ (dimen = 1,8-Diisocyanomenthane). *Inorg. Chem.* **1996,** *35*, 7704-7708.

14. Rodman, G. S.; Bard, A. J., Electrogenerated Chemiluminescence. 52. Binuclear Iridium(I) Complexes. *Inorg. Chem.* **1990,** *29*, 4699-4702.

15. Miskowski, V. M.; Smith, T. P.; Loehr, T. M.; Gray, H. B., Properties of Metal-Metal Single Bonds. Vibrational and Electronic Spectra of Binuclear Rhodium(II) and Iridium(II) Isocyanide Complexes with Comparisons to $Mn_2(CO)_{10}$. *J. Am. Chem. Soc.* **1985,** *107*, 7925-7934.

16. Che, C.-M.; Butler, L. G.; Grunthaner, P. J.; Gray, H. B., Chemistry and Spectroscopy of Binuclear Platinum Diphosphite Complexes. *Inorg. Chem.* **1985,** *24*, 4662-4665.

17. Bryan, S. A.; Schmehl, R. H.; Roundhill, D. M., Electrochemical oxidation of the tetrakis(m-pyrophosphito-*P*,*P'*)diplatinum(II) complex $Pt_2(m\text{-}P_2O_5H_2)_4^{4-}$ both in the presence and the absence of halide ions and reduction of the axially substituted halodiplatinum(III) complexes $Pt_2(m\text{-}P_2O_5H_2)_4X_2^{4-}$ *J. Am. Chem. Soc.* **1986,** *108*, 5408–5412.

18. Rhodes, M. R.; Mann, K. R., Electrochemical Oxidation of Tetrakis(1,8-diisocyanomenthane)dirhodium(2+) in Nonaqueous Solutions: A Net Two-Electron Oxidation Process. *Inorg. Chem.* **1984,** *23*, 2053-2058.

19. Kim, J.; Fan, F. F.; Bard, A. J.; Che, C.-M.; Gray, H. B., Electrogenerated chemiluminescence on the electrogenerated chemiluminescence (ECL) of tetrakis(pyrophosphito)diplatinate(II), $Pt_2(P_2O_5H_2)_4^{4-}$. *Chem. Phys. Lett.* **1985,** *121*, 543-546.

20. Vogler, A.; Kunkely, H., Electrochemiluminescence of Tetrakis(diphosphonato)diplatinate(II). *Angew. Chem. Int. Ed. Engl.* **1984,** *23*, 316-317.

21. Perdew, J. P.; Burke, K.; Ernzerhof, M., Generalized Gradient Approximation Made Simple. *Phys. Rev. Lett.* **1996,** *77*, 3865-3868.

22. Adamo, C.; Barone, V., Toward reliable density functional methods without adjustable parameters: The PBE0 model. *J. Chem. Phys.* **1999,** *110*, 6158-6170.

23. Grimme, S.; Antony, J.; Ehrlich, S.; Krieg, H., A consistent and accurate ab initio parameterization of density functional dispersion correction (DFT-D) for the 94 elements H-Pu. *J. Chem. Phys.* **2010,** *132*, 154104.

24. Záliš, S.; Ben Amor, N.; Daniel, C., Influence of the Halogen Ligand on the Near-UV-Visible Spectrum of [Ru(X)(Me)$(CO)_2$(a-diimine)] (X = Cl, I, a-Diimine = Me-DAB, iPr-DAB, DAB = 1,4-Diaza-1,3-butadiene): An ab Initio and TD-DFT Analysis. *Inorg. Chem.* **2004,** *43*, 7978-7985.

25. Záliš, S.; Lam, Y. C.; Gray, H. B.; Vlček, A., Jr., Spin−Orbit TDDFT Electronic Structure of Diplatinum(II,II) Complexes. *Inorg. Chem.* **2015,** *54*, 3491−3500.

26. Kvapilová, H.; Sattler, W.; Sattler, A.; Sazanovich, I. V.; Clark, I. P.; Towrie, M.; Gray, H. B.; Záliš, S.; Vlček, A., Electronic Excited States of Tungsten(0) Arylisocyanides. *Inorg. Chem.* **2015,** *54*, 8518−8528.

27. Tomasi, J.; Mennucci, B.; Cammi, R., Quantum Mechanical Continuum Solvation Models. *Chem. Rev.* **2005,** *105*, 2999-3093.

28. Ditchfield, R.; Hehre, W. J.; Pople, J. A., Self-Consistent Molecular Orbital Methods. 9. Extended Gaussian-type basis for molecular-orbital studies of organic molecules. *J. Chem. Phys.* **1971,** *54*, 724-728.

29. Raghavachari, K.; Binkley, J. S.; Seeger, R.; Pople, J. A., Self-consistent molecular orbital methods. XX. A basis set for correlated wave functions *J. Chem. Phys.* **1980,** *72*, 650-654.

30. McLean, A. D.; Chandler, G. S., Contracted Gaussian-basis sets for molecular calculations. 1. 2nd row atoms, Z=11-18. *J. Chem. Phys.* **1980,** *72*, 5639-5648.

31. Andrae, D.; Häussermann, U.; Dolg, M.; Stoll, H.; Preuss, H., Energy-adjusted ab initio pseudopotentials for the second and third row transition elements. *Theor. Chim. Acta* **1990,** *77*, 123-141.

32. Martin, J. M. L.; Sundermann, A., Correlation consistent valence basis sets for use with the Stuttgart–Dresden–Bonn relativistic effective core potentials: The atoms Ga–Kr and In–Xe. *J. Chem. Phys.* **2001,** *114*, 3408-3420.

33. Laury, M. L.; Carlson, M. J.; Wilson, A. K., Vibrational Frequency Scale Factors for Density Functional Theory and the Polarization Consistent Basis Sets. *J. Comput. Chem.* **2012,** *33*, 2380–2387.

34. Merrick, J. P.; Moran, D.; Radom, L., An Evaluation of Harmonic Vibrational Frequency Scale Factors. *J. Phys. Chem. A* **2007,** *111*, 11683-11700.

35. Exstrom, C. L.; Britton, D.; Mann, K. R.; Hill, M. G.; Miskowski, V. M.; Schaefer, W. P.; Gray, H. B.; Lamanna, W. M., Structures of $[M_2(dimen)_4](Y)_2$ (M = Rh, Ir; dimen = 1,8-Diisocyanomenthane; Y = PF_6, Tetrakis[3,5-bis(trifluoromethyl)phenyl]borate, $B(C_6H_5)_4$) Crystals Featuring an Exceptionally Wide Range of Metal-Metal Distances and Dihedral Twist Angles. *Inorg. Chem.* **1996,** *35*, 549-550.

36. Hunter, B. M.; Villahermosa, R. M.; Exstrom, C. L.; Hill, M. G.; Mann, K. R.; Gray, H. B., M−M Bond-Stretching Energy Landscapes for $M_2(dimen)_4^{2+}$ (M = Rh, Ir; dimen = 1,8-Diisocyanomenthane) Complexes. *Inorg. Chem.* **2012,** *51*, 6898−6905.

37. Hartsock, R. W.; Zhang, W.; Hill, M. G.; Sabat, B.; Gaffney, K. J., Characterizing the Deformational Isomers of Bimetallic $Ir_2(dimen)_4^{2+}$ (dimen = 1,8-diisocyano-p-menthane) with Vibrational Wavepacket Dynamics. *J. Phys. Chem. A* **2011,** *115*, 2920–2926.

38. Grimme, S.; Antony, J.; Ehrlich, S.; Krieg, H., A consistent and accurate ab initio parametrization of density functional dispersion correction (DFT-D) for the 94 elements H-Pu. *J. Chem. Phys.* **2010,** *132*, 154104.

39. Haldrup, K.; Harlang, T.; Christensen, M.; Dohn, A.; van Driel, T. B.; Kjær, K. S.; Harrit, N.; Vibenholt, J.; Guerin, L.; Wulff, M.; Nielsen, M. M., Bond Shortening (1.4 A) in the Singlet and Triplet Excited States of $[Ir_2(dimen)_4]^{2+}$ in Solution Determined by Time-Resolved X-ray Scattering. *Inorg. Chem.* **2011,** *50*, 9329–9336.

40. Grimme, S.; Djukic, J.-P., Cation-Cation "Attraction": When London Dispersion Attraction Wins over Coulomb Repulsion. *Inorg. Chem.* **2011,** *50*, 2619–2628.

41. Mann, K. R.; Gordon II, J. C.; Gray, H. B., Characterization of Oligomers of Tetrakis(phenyl isocyanide)rhodium(I) in Acetonitrile Solution. *J. Am. Chem. Soc.* **1975,** *97*, 3553-3555.

42. Smith, D. C.; Miskowski, V. M.; Mason, W. R.; Gray, H. B., Electronic Absorption and MCD Spectra of $M_2(TMB)_4^{2+}$, M = Rh and Ir. A Valence-Bond Description of the Upper Electronic Excited States. *J. Am. Chem. Soc.* **1990,** *112*, 3759-3767.